JOURNAL OF PROPULSION AND POWER
Vol. 17, No. 5, September–October 2001

Hybrid (Particle–Fluid) Modeling of Pulsed Plasma Thruster Plumes

Nikolaos A. Gatsonis* and Xuemin Yin†
Worcester Polytechnic Institute, Worcester, Massachusetts 01609

Integration of a pulsed plasma thruster (PPT) onboard spacecraft requires the evaluation of potential plume/spacecraft interactions that can be determined through plume modeling and characterization. A PPT plume model, numerical results, and comparisons with experiments are presented. The physical characteristics of PPT plumes are reviewed first, and the outstanding modeling issues related to the unsteady, partially ionized, collisional PPT plume plasma are presented. The PPT plume model is axisymmetric and based on a hybrid particle–fluid approach. Neutrals and ions are modeled with a combination of the direct simulation Monte Carlo and a hybrid-particle-in-cell method. Electrons are modeled as a massless fluid with a momentum equation that includes electric fields, pressure gradients, and collisional contributions from ions and neutrals. The nontime-counter methodology is used for neutral–neutral, elastic ion–neutral, and charge-exchange collisions. Ion–electron collisions are modeled with the use of a collision force field. Electric fields are obtained from a charge conservation equation under the assumption of quasi neutrality. The code incorporates subcycling for the time integration and unsteady particle injection. Simulations are performed using PPT conditions representative of a NASA John H. Glenn Research Center at Lewis Field laboratory-model PPT operating at discharge energies of 5, 20, and 40 J. The results demonstrate the expansion of the neutral and ion components of the plasmoid during a pulse, the generation of low-energy ions and high-energy neutrals due to charge-exchange reactions, and the generation of neutral and ion backflow. Numerical predictions are compared with unsteady plume electron density data and show good quantitative agreement. Backflow predictions are presented for the three discharge energy levels considered.

Nomenclature

a_0	=	Bohr radius, 5.2918×10^{-11} m
$\boldsymbol{B}$	=	magnetic induction field vector, T
$\bar{c}_s$	=	mean speed of species s, ms^{-1}
d_{ref}	=	molecular diameter at the reference temperature, m
$\boldsymbol{E}$	=	electric field, Vm^{-1}
e	=	elementary charge, 1.6022×10^{-19} C
$\boldsymbol{F}_{ie}$	=	i–e collision force, N
g	=	relative speed between two colliding particles
I_{bit}	=	impulse bit, N · s
I_{sp}	=	specific impulse, s
$\boldsymbol{J}$	=	current density vector, Am^{-2}
k	=	Boltzmann constant, 1.3807×10^{-23} JK^{-1}
L	=	characteristic length
L_Z, L_R	=	axial and radial size of the simulation domain, m
M_A	=	propellant mass ablated (injected) during a pulse, kg
$M_{I,N}$	=	total ion (neutral) mass ablated (injected) during a pulse, kg
$M_{i,n}$	=	ion i (neutral n) mass ablated (injected) during a pulse, kg
m_e	=	9.1094×10^{-31} kg
m_s	=	particle mass of species s, kg
$\dot{m}_s$	=	species s mass flow rate, $\mathrm{kgs}^{-1}\mathrm{m}^{-2}$
N_s	=	total number of computational macroparticles of species s
$\dot{N}_s$	=	number flux of species s particles
$n_{s,\max}$	=	maximum number density of species s, m^{-3}
$n_s(\boldsymbol{r}, t)$	=	number density of species s, m^{-3}
n_0	=	background plasma density, m^{-3}
P	=	pulse duration, s
p_s	=	kinetic pressure of species s, Nm^{-2}
R, Z	=	radial and axial distances in the axisymmetric coordinate system, m
R_T	=	equivalent thruster radius, m
r, θ	=	polar coordinates measured from center of Teflon® bar, cm and deg
S_s	=	speed ratio
s	=	species type, i for ions and n for neutrals
T_{ref}	=	reference temperature, K
T_s	=	temperature of species s, K
$U_{i,n}$	=	average drift velocity at the pulsed plasma thruster exit
u_s, v_s, w_s	=	axial, radial, and azimuthal drift components, ms^{-1}
$\boldsymbol{u}_s$	=	average (drift) particle velocity for species s particles, $\langle \boldsymbol{v}_s \rangle$
$V_{e,i,n}$	=	characteristic velocity for electrons, ions, and neutrals
$\boldsymbol{v}_s$	=	particle velocity of species s
W_s	=	molecular weight of species s particle
X_s	=	species s mass fraction with respect to the total mass
$\boldsymbol{x}_s$	=	particle position vector
Z_i	=	number charge of ion i
α_R	=	relative polarizability
ΔZ, ΔR	=	axial and radial cell width, m
ε_0	=	permittivity of free space, 8.854×10^{12} Fm^{-1}
η	=	total propellant ionization fraction
Λ_{ie}	=	Coulomb logarithm
λ_D	=	debye length, m
λ_{st}	=	mean-free path for collisions between s and t, m
ν_e	=	total electron collision frequency, s^{-1}
ν_{ie}^{ε}	=	average i–e energy transfer collision frequency, s^{-1}
ν_{st}	=	average momentum transfer collision frequency for collisions between s and t, s^{-1}
ρ_c	=	charge density, Cm^{-3}

Received 11 May 1999; revision received 1 December 1999; accepted for publication 8 February 2001. Copyright © 2001 by Nikolaos A. Gatsonis and Xuemin Yin. Published by the American Institute of Aeronautics and Astronautics, Inc., with permission.

*Associate Professor, Computational Gas and Plasma Dynamics Laboratory, Mechanical Engineering Department, 100 Institute Road. Senior Member AIAA.

†Graduate Research Assistant, Computational Gas and Plasma Dynamics Laboratory, Mechanical Engineering Department, 100 Institute Road; currently Software Engineer, Nortel Networks, 600 Technology Park Drive, Billerica, MA 01821. Member AIAA.

σ_{in}^{M} = momentum transfer cross section for elastic i–n collisions, m^2
$\sigma_{in}^{M,CEX}$ = momentum transfer cross section for charge-exchange i–n collisions, m^2
σ_T = total cross section for elastic n–n collisions, m^2
τ = characteristic time
ϕ = electric potential, V
ω = index of the viscosity–temperature power law used in the variable hard sphere model

Introduction

THE pulsed plasma thruster (PPT) is an electromagnetic thruster that uses solid Teflon® for propellant. PPTs can deliver high specific impulses of up to 1000 s, have low electric power requirements (<150 W), and have a very simple propellant system. These characteristics make them an attractive and reliable onboard propulsion option. Potential applications include orbit maintenance, attitude control, orbit insertion, and deorbiting for both large- and small-satellite missions. As with any propulsion technology, successful integration and operation of PPTs on spacecraft require the complete assessment of the environment induced by PPT plumes, as well as the potential for spacecraft interactions. The characteristics of PPT plumes are quite distinct when compared to other electric or chemical thrusters. PPTs produce thrust by the acceleration of ablated Teflon during a pulsed discharge of an energy storage capacitor. The arc discharge lasts several microseconds and ablates several micrograms of the Teflon propellant. The force resulting from the interaction between the current and the induced magnetic field accelerates the generated plasma outside the thruster. Only a portion of the ablated mass of the propellant becomes ionized. Therefore, PPT plumes are composed of various ion and neutral species due to propellant decomposition. In addition, they contain nonpropellant efflux due to thruster materials, electromagnetic efflux, and optical emissions. PPT plumes are inherently unsteady because of the interaction of individual plasmoids during the pulsed operation of the thruster. Physical modeling of PPT plumes is limited, and simulation of such a partially ionized, collisional, and high-density plasma is very challenging. Because of the projected use of PPTs, it is important to further investigate their plumes and develop a predictive ability that will determine the potential for spacecraft interactions. The motivation of our study is to develop a physical and computational model capable of addressing the complex, partially ionized PPT effluent environment.[1–3] Our modeling effort, along with plume characterization efforts, will provide the much needed predictive capability.[4–7]

In this paper we review first the PPT plume components and the computational issues involved in plume modeling. We then present the physical plume model, which is based on a hybrid description of the partially ionized plasma. We summarize the hybrid computational methodology that combines concepts from the direct simulation Monte Carlo (DSMC), a hybrid-particle-in-cell (hybrid-PIC), and fluid techniques. We then present simulation results using an injection model with parameters representative of the NASA John H. Glenn Research Center at Lewis Field (GRC) PPT at discharge energy levels of 5, 20, and 40 J. We investigate the complex plasmadynamic processes that occur in the PPT plume. We present extensive comparisons between model predictions and triple langmuir probe plume measurements.[6,7] Finally, we present and discuss backflow predictions.

PPT Plume Effluents, Modeling Issues, and Approach

A review of the PPT literature reveals an early awareness for the assessment of plume contamination. PPT plume characterization has been challenging because it requires development of special diagnostic techniques to cope with the intricacies of the plume. The majority of the available ground-based investigations was conducted in the early 1970s using the Lincoln Experimental Sattelite-6 (LES-6) thruster[8–11] or specifically designed PPTs,[12,13] with fewer studies appearing in the 1980s.[14,15] The renewed interest in PPTs[16] prompted new plume investigations, using a derivative of the flight-qualified LES-8/9.[4–7,17,18] As a result of these experimental investigations, various aspects of PPT plumes and contamination issues have been addressed. We will review these plume investigations to provide the necessary background and discuss the issues relevant to modeling.

PPT plumes consist of neutral, single-, and multiple-ionized C, F, and C_xF_y species resulting from the partial decomposition of Teflon.[5,10,14,15] In addition, particles from eroded thruster materials have been identified in the plume.[5,15,18] Species production in the PPT channel is time dependent and species populations have different mean velocities and temperatures. A spectroscopic study of the LES-6 plume by Thomassen and Vondra[10] identified velocities of 4000 m/s for F and 35,000 m/s for C^{+++}. Dawbarn et al.,[14] using a PPT with ablated mass of $M_a = 1.71$ μg/pulse and a period of $P = 50$ μs, observed two ion plasmoids moving with 40 and 13 km/s, respectively. Using the LES-8/9 PPT, Eckman et al.[5] showed that the plasmoid produced during the PPT pulse consists of two ion peaks with an average ion speed of 60 and 30 km/s, respectively. The most comprehensive electron density and temperature measurements obtained by Eckman et al.[6] using triple langmuir probes in the plume of a GRC PPT operated at discharge energy levels of $E_D = 5$, 20, and 40 J. Measurements were taken at a range of positions within 20 cm downstream of the Teflon propellant and at angular locations from 0 to 45 deg with respect to the centerline. Plume properties showed large angular variation on the perpendicular to the electrodes plane, but small variation on the parallel plane, confirming the asymmetry of the PPT plume. The maximum electron densities ranged from 1×10^{19} to 3×10^{21} m^{-3}, and instantaneous electron temperatures were between 1 and 5 eV for all discharge energy levels considered. Despite the numerous ground- based investigations, the characterization of the plume species is far from being complete. Fast- moving ions appear to explain the thrust derived by PPTs, but there is little information on the relevant contribution of the multiple-ionized components of the charged efflux. Overall, the composition and plume properties depend on thruster operating conditions.

It has also been established that neutral particles continue to leave the thruster well after the passage of ions, but there is a fast-moving neutral component as well. Fast ionization gauge data of Eckman et al.[5] show that the neutrals in the plume of an LES-8/9 flow for up to 2 ms after the initiation of the 12-μs pulse and travel with much lower speeds than the ions. Analysis indicates that a significant fraction of the plume mass is relatively slow moving and is at a low temperature. Therefore, gasdynamic effects related to the low-energy portion of the plume can be important on the backflow of material. The exact composition of the neutral effluxes and their contribution to the thrust are still not known.

Chemical interactions among the Teflon species in the plume have not been investigated so far. The potential for plume/spacecraft interactions depends on the characteristics of each population: The high-energy particles, for example, can not contribute to spacecraft interactions unless they are impinging spacecraft surfaces directly. However, secondary interactions that lead to the generation of low-energy species need to be investigated. Such interactions include charge-exchange reactions, which have been thoroughly studied for ion thrusters but not for PPTs.

Note that the extensive flight heritage of PPTs showed no adverse effects on spacecraft operation. The NOVA PPTs with a peak power level of 30 W, I_{sp} of 543 s, I_{bit} of 400 mN · s, and a combined operation of over 20 years, showed no observed impact on solar arrays or other spacecraft operations.[19] The LES, launched in 1968, used four experimental PPTs for station keeping flawlessly for almost 9000 h (Ref. 19). However, ground-based and flight results cannot be scaled easily to new designs or more powerful PPTs planned for future missions.

Based on our current understanding, it can be argued that PPT plumes are more complex than other electric or chemical thrusters due to the presence of a neutral and an ionized component, as well as their unsteady character. PPT plumes fall in the category of high-density, collisional, and partially ionized plasmas. As the following review demonstrates, computational methodologies for these plasmas are still under development.

Simulation of neutral plumes is a very mature field, with Navier–Stokes solvers covering the continuum regime, DSMC solvers covering the transitional to rarefied regimes, and combinations of the two covering both regimes.[20–25] Fully ionized but low-density collisionless plasma plumes could be modeled with the PIC method.[26,27] To alleviate difficulties associated with electron time steps and debye-length limitations, various formulations of PIC/fluid (hybrid) methodologies have been developed and used in a variety of plume problems. A hybrid methodology using a PIC model for ions, Boltzmann electrons, and an analytical model for neutrals has been used successfully in the simulation of ion thruster plumes.[28,29] Subsequent studies of nuclear thermal rocket plumes,[30] Hall thruster plumes,[31,32] and PPT plumes[1–3] utilized the DSMC for neutrals and PIC for ions, but retained the Boltzmann model for the electrons and obtained electric fields from Poisson's equation. Finally, purely fluid approaches have been used to address large-scale plasma plumes.[33]

In this study we present the first comprehensive hybrid physical and computational model of a PPT plume, simulation results, and comparisons with data. Unlike other DSMC/PIC plume studies[28–32] and our previous work[1,2] that utilized the Boltzmann approximation for the electrons, in this work electrons are modeled as a massless fluid with a momentum equation that includes collisional contributions from ions and neutrals. The unsteady character of the plume is considered as a series of plasmoids ejected from the exit of the thruster channel during the thruster firing. The plume model includes neutrals, for example C and F, and ions, for example, C^+ and F^+, from the Teflon decomposition. A hybrid representation is chosen to model the physical characteristics of the PPT plume components. Neutrals and ions are treated as particles using concepts of the DSMC[20] and a hybrid-PIC[26,27,34] approach that includes a collisional ion–electron force. The kinetic description of ions and neutrals is necessary and will allow evaluation of fluxal properties needed for future contamination characterization. Charge-exchange interactions are included to assess the potential for generation of a low-energy charge-exchange plasma. Electric fields are obtained from a formulation of the current conservation equation that allows discretization at scales larger than the debye lengths, thus alleviating computational restrictions at the high densities of PPT plumes. The code incorporates a single grid and subcycling for the time integration. Collisional interactions such as neutral–neutral and ion–neutral, including charge exchange, are modeled using the nontime counter method (NTC).[20]

Hybrid Plume Model

The simulation domain shown in Fig. 1 represents an axisymmetric region with the downstream (axial direction) designated by Z and the radial direction by R. The bottom boundary is the centerline of the plume and is the axis of symmetry. The downstream, top, and upstream boundaries are placed at distances far enough to include the plume and to account for the investigation of backflow. The background plasma is treated as a stationary medium with constant density n_∞. At the thruster exit, particles enter the domain with prescribed density, velocity, or flux distributions. These profiles can be specified from either experimental observations or internal flow models. Species in the model include 1) neutrals, 2) ions, 3) charge-exchange ions and neutrals, and 4) electrons.

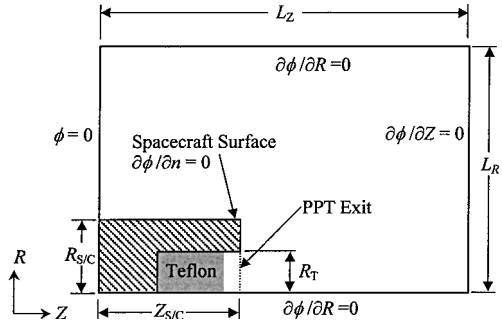

Fig. 1 Axisymmetric simulation domain.

DSMC/Hybrid-PIC Model for Ions and Neutrals

Ion and neutral plume species are modeled using concepts of a hybrid-PIC and the DSMC methodologies. The distribution function of a plume species s (i, n) with mass m_s is given by a local Maxwellian

$$f_s(\boldsymbol{r}, \boldsymbol{v}, t) = n_s(\boldsymbol{r}, t)\left(\frac{m_s}{2\pi k T_s}\right)^{\frac{3}{2}} \exp\left[-\frac{m_s(\boldsymbol{v}_s - \boldsymbol{u}_s)^2}{2kT_s}\right] \quad (1)$$

where m_s is the mass, $\boldsymbol{v}_s$ the particle velocity, $n_s(\boldsymbol{r}, t)$ the number density, $\boldsymbol{u}_s(\boldsymbol{r}, t) = \langle \boldsymbol{v}_s \rangle \equiv (u_s, v_s, w_s)$ the average (or drift) species velocity (brackets indicate average over the species distribution function), T_s the temperature, and k the Boltzmann constant. Each species s macroparticle (or simulation particle) represents F_s number of real plume particles. A total of N_s macroparticles reside in the simulation domain with the kth macroparticle described by a set of position and velocity $\{\boldsymbol{x}_{sk}, \boldsymbol{v}_{sk}\}$ $k = 1, N_s$. Neutral and ion particles move and undergo collisions that include neutral–neutral elastic, ion–neutral elastic, ion–neutral charge exchange, and ion–electron.

The simulation domain in Fig. 1 is discretized using a structured nonuniform grid with a total of N_Z and N_R cells in the axial and radial directions, respectively. Following the DSMC methodology, the cell widths scale with the local mean-free path, $\lambda_{st} = \bar{c}_s/\nu_{st}$, defined as the ratio of the species mean speed $\bar{c}_s = \sqrt{(8kT_s/\pi m_s)}$ to the average collision frequency ν_{st}. Cells are also further divided in subcells and used for the evaluation of collisions.[20] The vertices of each cell are the nodes where the average (fluid) quantities are evaluated. Details of the grid generation are presented along with the numerical simulations.

Neutral–Neutral Collisions

The modeling of neutral particle collisions and motion is accomplished by the NTC method described by Bird.[20] The variable hard sphere model is used to model neutral–neutral collisions. The total cross section for neutral particle collisions is

$$\sigma_T = \pi d_{\text{ref}}^2 \left(2kT_{\text{ref}}/m_r g^2\right)^{\omega - \frac{1}{2}} \Gamma\left(\tfrac{5}{2} - \omega\right)^{\frac{1}{2}} \quad (2)$$

where d_{ref} is the reference diameter at the reference temperature T_{ref}, $m_r = m_s m_t/(m_s + m_t)$ is the reduced mass, g is the relative speed, and ω is the index of the viscosity–temperature power law. For C and F neutral species used in the simulations, $d_{\text{ref}}(\text{F}) = 3.0 \times 10^{-10}$ m, $d_{\text{ref}}(\text{C}) = 2.5 \times 10^{-10}$ m, and $\omega = 0.75$. Postcollision velocities are obtained from momentum and energy consideration. When multiatomic molecules are included in the plume, the internal energy of the collision partners is redistributed following the Larsen–Borgnakke model (see Ref. 20).

Ion–Neutral Elastic Collisions

Elastic ion–neutral collisions are treated similarly to the neutral–neutral ones using the NTC methodology. The momentum transfer cross section used in the determination of the collision probability can be expressed as[35,36]

$$\sigma_{\text{in}}^M = \sqrt{\pi \alpha_R a_0^3 e^2 \big/ \varepsilon_0 m_r}\,(1/g) \quad (3)$$

where α_R is the relative polarizability and $a_0 = 5.2918 \times 10^{-11}$ m is the Bohr radius. The relative polarizibility is 12 for C and 3.8 for F. The occurrence of a collision is based on the available relative energy, which has to be below a specified threshold E_{cx}.

Ion–Neutral Resonant Charge-Exchange Collisions

Ions and neutrals in the model include those created by the charge-exchange (CEX) reaction

$$\text{X}^n_{\text{slow(fast)}} + \text{X}^+_{\text{fast(slow)}} \longrightarrow \text{X}^n_{\text{fast(slow)}} + \text{X}^+_{\text{slow(fast)}} \quad (4)$$

The low-energy CEX species are of particular importance to backflow and possible spacecraft contamination. It has been shown that in ion thruster plumes, low-energy ions can be strongly affected by

Table 1 Constants in the CEX cross section expression

Reaction	A	B
F^+–F	8.3343×10^{-19}	-1.2522×10^{-19}
C^+–C	1.7771×10^{-18}	-2.6797×10^{-19}

the self-induced electric fields in the plume and accelerate outside the plume in the radial and the backflow directions.[27,28] The preceding CEX reaction can be expressed by a momentum transfer cross section from Sakabe and Izawa[37] as

$$\sigma_{\text{in}}^{M,\text{CEX}} = A + B\log(g) \tag{5}$$

where the coefficients A and B are listed in Table 1. The NTC methodology is used to determine the number of possible CEX partners in each cell with the cross section given in Eq. (5). Because of the nature of the CEX collision, the postcollision velocities of the reacting particles are simply exchanged.

Ion and Neutral Particle Motion

After the collision process has been completed in all cells, a particle with a postcollision velocity $\boldsymbol{v}_s$ is moved according to

$$\frac{\mathrm{d}\boldsymbol{x}_s}{\mathrm{d}t} = \boldsymbol{v}_s \tag{6}$$

For an ion particle with position $\boldsymbol{x}_i$ and charge q_i, the equation of motion includes the electric field force $q_i\boldsymbol{E}$, as well as a collision force $\boldsymbol{F}_{ie}$,

$$m_i\frac{\mathrm{d}\boldsymbol{v}_i}{\mathrm{d}t} = q_i\boldsymbol{E}(\boldsymbol{x}_i) + \boldsymbol{F}_{ie}(\boldsymbol{x}_i) \tag{7}$$

The integration of the equation of motion (5) and (6) of a neutral or an ion particle in axisymmetric coordinates takes into account the azimuthal component of the velocity following standard procedures.[20,26]

Induced magnetic fields are not included in the equation of ion or electron motion. Magnetic field measurements for our laboratory model PPT or other LES derivatives are not available. Estimates of self-induced magnetic fields inside a rectangular-geometry PPT that may diffuse into the plume region depend solely on the internal flow, which is still a subject of investigation. The most recent internal flow model[38] provides insights on the structure of the internal magnetic fields in a rectangular-geometry PPT. The analytical model[38] reproduced key PPT parameters under the assumption that the induced $\boldsymbol{B}$ field is zero at the end of the discharge zone, well before the thruster exit. Finally, note that inclusion of self-induced magnetic fields in our plume simulations would require the development of an electromagnetic hybrid model that is outside the scope of this work.

Ambient magnetic fields are also neglected based on estimates of ion magnetization using values of the ambient magnetic induction $|\boldsymbol{B}|\approx10^{-5}$ T in low Earth orbit (LEO) and $|\boldsymbol{B}|\approx10^{-7}$ T in geosynchronous Earth orbit (GEO). With the ambient $\boldsymbol{B}$ values, thermal plume ions with $\bar{c}_i = \sqrt{(8kT_i/\pi m_i)}$ will have gyroradii larger than a meter, and primary ions with $|\boldsymbol{u}_i|\sim10^4$ ms^{-1} will have gyroradii larger than hundreds of meters. Thus, for the meter-size length scales of interest in our study, the ions can be considered to be unmagnetized.

The electric field and the collision force in Eq. (7) needed at the ion position $\boldsymbol{x}_i$ are evaluated from the cell-vertex (nodal) values using an axisymmetric conservative weighting scheme.[39] The evaluation of the electric field at the nodes is provided by a current conservation model and is discussed later. The collision force at the nodes incorporates ion–electron collisions into the PIC method and is given by Jones et al.[34] as

$$\boldsymbol{F}_{ie} = \nu_{ie}m_{ie}(\langle\boldsymbol{v}_e\rangle - \langle\boldsymbol{v}_i\rangle) + \left(\frac{\nu_{iek}^{\varepsilon}(T_i-T_e)}{\langle\boldsymbol{v}_i^2\rangle - \langle\boldsymbol{v}_i\rangle^2} - \frac{\nu_{ie}m_{ie}^2(\langle\boldsymbol{v}_e\rangle - \langle\boldsymbol{v}_i\rangle)^2}{m_i\left(\langle\boldsymbol{v}_i^2\rangle - \langle\boldsymbol{v}_i\rangle^2\right)}\right)(\langle\boldsymbol{v}_i\rangle - \boldsymbol{v}_i) \tag{8}$$

where $m_{ie} = m_im_e/(m_i+m_e)$ is the reduced mass and brackets indicate averaging over the species distribution function. The average (or fluid) ion quantities in Eq. (8) $\langle\boldsymbol{v}_i\rangle = \boldsymbol{u}_i$, $\langle\boldsymbol{v}_i^2\rangle$ and $\langle\boldsymbol{v}_i\rangle^2$, and T_i are obtained at a grid point from interpolation of all particles in the surrounding cells using the axisymmetric weighting scheme.[38] The average velocity of electrons at a grid point $\langle\boldsymbol{v}_e\rangle = \boldsymbol{u}_e$ is obtained from the fluid model described hereafter. The dynamic friction collision frequency in Eq. (8) is given by[34]

$$\nu_{ie} = \frac{8\sqrt{\pi}}{1}\left(\frac{Z_ie^2}{4\pi\varepsilon_0m_e}\right)^2\frac{1}{(\Delta u)^3}n_e\,\ell n\Lambda_{ie} \times\left[\frac{\sqrt{\pi}}{2}\,\mathrm{erf}\left(\frac{\Delta u}{v_{th}}\right) - \left(\frac{\Delta u}{v_{th}}\right)\exp\left(\frac{-\Delta u^2}{v_{th}^2}\right)\right] \tag{9}$$

where $\Delta u = |\boldsymbol{u}_i - \boldsymbol{u}_e|$, $v_{th}^2 = 2k(T_i/m_i + T_e/m_e)$ and Λ_{ie} is the Coulomb logarithm. In the absence of relative drifts the preceding equation reduces to the well-known expression[40]

$$\nu_{ie} = \frac{16\sqrt{\pi}}{3}\left(\frac{Z_ie^2}{4\pi\varepsilon_0m_e}\right)^2\left(\frac{2kT_i}{m_i} + \frac{2kT_e}{m_e}\right)^{-\frac{3}{2}}n_e\,\ell n\Lambda_{ie} \tag{10}$$

The energy transfer collision frequency in Eq. (8) is

$$\nu_{ie}^{\varepsilon} = \frac{16\sqrt{\pi}}{1}\frac{Z_i^2e^4}{(4\pi\varepsilon_0)^2m_im_e} \times\left(\frac{2kT_i}{m_i} + \frac{2kT_e}{m_e}\right)^{-\frac{3}{2}}n_e\,\ell n\Lambda_{ie}\exp\left[-\left(\frac{\Delta u}{v_{th}}\right)^2\right] \tag{11}$$

Fluid Electron Model

The general form of the electron momentum equation is

$$\frac{\partial\boldsymbol{u}_e}{\partial t} + \boldsymbol{u}_e\cdot\nabla\boldsymbol{u}_e = -\frac{e}{m_e}(\boldsymbol{E}+\boldsymbol{u}_e\times\boldsymbol{B}) - \frac{1}{n_em_e}\nabla p_e - \sum_i\nu_{ei}(\boldsymbol{u}_e-\boldsymbol{u}_i) - \sum_n\nu_{en}(\boldsymbol{u}_e-\boldsymbol{u}_n) \tag{12}$$

The electron pressure is given by the ideal law $p_e = n_ekT_e$, $\nu_{ei} = \nu_{ie}$ is given by Eq. (9), and ν_{en} is given by many authors.[40] Estimates of the terms appearing in the momentum equation (12) can be obtained using scaling arguments. We assume that the characteristic length $L\sim10^{-1}$ m is based on the macroscopic length of a plasmoid and is given by the distance covered by a primary ion with $V_i\sim10^4$ ms^{-1} during a PPT pulse with characteristic time $\tau\sim10^{-5}$ s. We further assume that $n_e\sim10^{18}$–10^{21} m^{-3}; $T_e\sim1$–5 eV; $n_n\sim10^{18}$–10^{22} m^{-3}; the velocity of neutrals $V_n\sim10^3$–10^4 ms^{-1}; the electron thermal velocity $V_{th,e} = \sqrt{(kT_e/m_e)}\sim10^6$ ms^{-1}; the electron gyrofrequency $\omega_{ce} = eBm_e^{-1}\sim10^4$–$10^6$ s^{-1} for magnetic field intensities of $|\boldsymbol{B}|\approx10^{-7}$ T in GEO and $|\boldsymbol{B}|\approx10^{-5}$ T in LEO, respectively; $\nu_{ie}\sim3\times10^6$–2×10^{10} s^{-1}; and $\nu_{en}\sim10^5$–10^8 s^{-1}. The magnitude of $E\approx\Delta\phi L^{-1}$ where $\Delta\phi$ is in the range of 15–120 V based on $\Delta\phi\sim(kT_e/e)\,\ell n(n_e/n_{eo})$ and $n_{e0}\le10^{12}$ m^{-3} is the maximum ambient electron density at LEO.

With these scaling arguments, the unsteady term $\partial|\boldsymbol{u}_e|/\partial t\sim V_e\tau^{-1}V_e\tau^{-1}$ can be neglected in comparison to the electron–ion collision term $(\nu_{ei}+\nu_{en})V_e$ because $\tau\gg\nu_{ei}^{-1}$. The inertia term $|\boldsymbol{u}_e\cdot\nabla\boldsymbol{u}_e|\sim V_e^2L^{-1}$ can also be neglected in comparison with the pressure term $(n_em_e)^{-1}|\nabla p_e|\sim V_{th,e}^2L^{-1}$ because it is expected that $V_{th,e}>V_e$. The ratio of the electric to the magnetic component in the Lorentz term is given by $\Delta\phi/V_e|\boldsymbol{B}|L$. For magnetic field intensities of $|\boldsymbol{B}|\approx10^{-5}$ T in LEO and $|\boldsymbol{B}|\approx10^{-7}$ T in GEO, this ratio is much larger than unity, and, therefore, magnetic field effects on electron transport can be neglected in comparison to electric fields. The collisional terms

$$\sum(\nu_{ei}+\nu_{en})|\boldsymbol{u}_e|\sim(\nu_{ei}+\nu_{en})V_e$$

$$\sum_i\nu_{ei}|\boldsymbol{u}_i|\sim\nu_{ei}V_i\sum_n\nu_{en}|\boldsymbol{u}_n|\sim\nu_{en}V_n$$

can easily be of the same order as the pressure $(n_e m_e)^{-1}|\nabla p_e| \sim V_{th,e}^2 L^{-1}$ or the electric term $em_e^{-1}|\boldsymbol{E}| \sim em_e^{-1}\Delta\phi L^{-1}$.

Based on the scaling analysis, unsteady, inertia, and magnetic terms are ignored, and the electron momentum equation can be written in the following form:

$$\boldsymbol{u}_e = -\frac{e\boldsymbol{E}}{m_e \nu_e} - \frac{1}{n_e m_e \nu_e}\nabla p_e + \left(\sum_i \nu_{ei}\boldsymbol{u}_i \Big/ \nu_e\right) + \left(\sum_n \nu_{en}\boldsymbol{u}_n \Big/ \nu_e\right) \tag{13}$$

The total electron collision frequency in Eq. (13) is defined as

$$\nu_e = \sum_i \nu_{ei} + \sum_n \nu_{en} \tag{14}$$

The electron–neutral ionization frequency using the simple Thomson model (see Ref. 36) was estimated to be two to three orders of magnitudes smaller than ν_{ei} and was not included in the evaluation of the total collision frequency.

In cases where the collisional terms can be ignored in comparison to the pressure gradient or electric field, the electron momentum equation (13) reduces to the well-known Boltzmann expression. However, in the PPT plume, even at electron densities $n_e \leq 10^{17}$ m^{-3} where $\nu_{ei} \leq 10^5$ s^{-1}, it is possible for the e–n collisional terms $\nu_{en}V_e$ or $\nu_{en}V_n$ to become of the same order as the pressure gradient or the electric terms. Therefore, the full form of the reduced electron momentum equation (13) is used in this model.

The mean (fluid) ion $\boldsymbol{u}_i$ and neutral $\boldsymbol{u}_n$ velocities needed for the evaluation of $\boldsymbol{u}_e$ at a grid point according to Eq. (13) are obtained from interpolation of particle velocities in the surrounding cells. Electrons are assumed isothermal with a specified temperature T_e.

Plume Electrodynamics and Current Conservation

An important simplification in the model comes from the assumption of quasi neutrality, that is,

$$\rho_c = \sum_s q_s n_s \approx 0$$

where ρ_c is the charge density. This approximation is valid for length scales that are much larger than the debye length and is appropriate for the dense portions of the plume. However, it is violated near solid walls or the edges of the plume. The electron density in the quasi-neutral approximation is given by

$$n_e \cong \sum_i n_i \tag{15}$$

A major advantage in our approach is that electric fields are obtained from a charge-conservation formulation and not Poisson's equation as is traditional in PIC formulations. This approach allows discretization on scales larger than the local debye length λ_D, which, for plasma densities $n_e \approx 10^{17}$–10^{21} m^{-3} and $T_e \approx 1$–5 eV, is in the range of 10^{-5}–10^{-7} m. Current conservation under quasi neutrality can be written as

$$\nabla \cdot \boldsymbol{J} = 0 \tag{16}$$

where the total current density is

$$\boldsymbol{J} = \sum_s n_s q_s \boldsymbol{u}_s = \sum_i q_i n_i \boldsymbol{u}_i - e n_e \boldsymbol{u}_e \tag{17}$$

With Eqs. (13), (15), and (17), Eq. (16) can be rewritten as

$$\nabla \cdot \left(\frac{e^2 n_e}{m_e \nu_e}\boldsymbol{E}\right) = -\nabla \cdot \left(\sum_i n_i q_i \boldsymbol{u}_i\right) - \nabla \cdot \left(\frac{e}{m_e \nu_e}\nabla \cdot p_e\right) - \nabla \cdot \left[-en_e\left(\sum_i \nu_{ei}\boldsymbol{u}_i \Big/ \nu_e\right)\right] - \nabla \cdot \left[-en_e\left(\sum_n \nu_{en}\boldsymbol{u}_n \Big/ \nu_e\right)\right] \tag{18}$$

The quantities in the right-hand side of the equation provide the divergence of currents due to ion drift, pressure gradients, electron–ion, and electron–neutral collisions, respectively. The charge $n_e = n_i$ on the nodes is obtained through weighting of the charge of the particles found in the cells surrounding the node using a conservative weighting scheme.[39] We also neglect displacement currents in the plasma and induced magnetic fields. Therefore, electric fields are electrostatic, given by a potential ϕ as

$$\boldsymbol{E} = -\nabla\phi \tag{19}$$

The electric field is obtained on the grid points from finite differencing of Eq. (18). Boundary conditions used with Eq. (18) are shown in Fig. 1. Zero axial electric field is imposed along the downstream boundary and zero radial field along the axis centerline. At the upstream boundary the potential is set to zero. Along the top surface a zero field is imposed. The boundary condition at the thruster exit can be derived from the exit flow conditions. For example, for given total current density at the exit $\boldsymbol{J}_E(R, Z_E, t) = 0$, the electric field can be derived analytically using Eqs. (13) and (17).

The loading of particles follows standard procedures.[20,26,27] Particles reaching the far-field boundaries from inside the domain are removed from the simulation, and those passing across the centerline are reflected back to represent the axisymmetry condition. The top surface of the channel is set to an absorption condition where the particles are assumed to be deposited onto the surface.

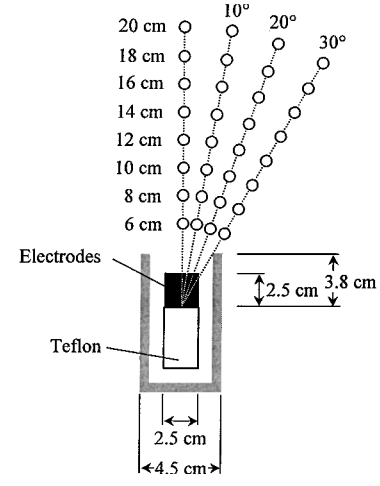

Perpendicular plane view

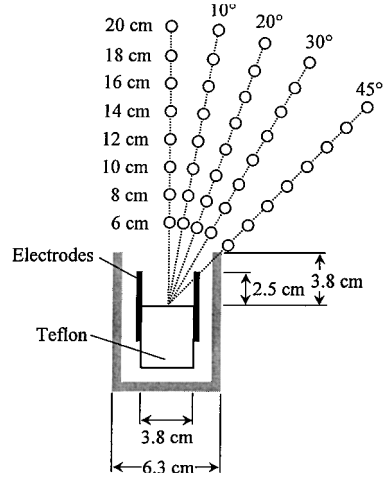

Parallel plane view

Fig. 2 Schematic of NASA GRC laboratory-model PPT used in triple probe experiments; measurements were taken along designated polar angles θ = 10, 20, and 30 deg and for distances r from 6 to 20 cm from the Teflon propellant.

Thruster Exit (Injection) Model

Particle injection at the PPT thruster exit (R, Z_E) requires the evaluation of the number flux of each species s (i or n) expressed by

$$\dot{N}_s(R, Z_E, t) = \tfrac{1}{4} n_s(R, Z_E, t)\bar{c}_s\left\{\exp\left(-S_s^2\right) + \sqrt{\pi} S_s[1 + \operatorname{erf}(S_s)]\right\} \tag{20}$$

where the speed ratio is $S_s = u_s/\sqrt{(2kT_s/m_s)}$. It is, therefore, necessary to obtain $n_s(R, Z_E, t)$, $\boldsymbol{u}_s(R, Z_E, t)$, and $T_s(R, Z_E, t)$ at the exit to proceed with the particle injection. Ideally, this should be given from PPT thruster exit data or internal PPT modeling. Such data are not available, and an injection (thruster exit) model is necessary to include as much information as possible from measurements.

Our injection model proceeds with the assumption that the Teflon is decomposed during the PPT discharge according to

$$a\,\mathrm{C_2F_4} \rightarrow b\,\mathrm{C} + c\,\mathrm{C^+} + d\,\mathrm{F} + e\,\mathrm{F^+} \tag{21}$$

The total injected (ablated) mass M_A over the pulse duration P is given as

$$M_A = \sum_i M_i + \sum_n M_n = M_I + M_N = aW_{\mathrm{C_2F_4}} \tag{22}$$

where $W_{\mathrm{C_2F_4}}$ is the molecular weight of Teflon. Following Eq. (21) and the definition of a species fraction $X_s = M_s/M_A$, the mass-balance equations are written as

$$X_{\mathrm{C^+}} + X_{\mathrm{C}} = 2W_{\mathrm{C}}/W_{\mathrm{C_2F_4}} \tag{23}$$

$$X_{\mathrm{F^+}} + X_{\mathrm{F}} = 4W_{\mathrm{F}}/W_{\mathrm{C_2F_4}} \tag{24}$$

$$X_{\mathrm{C^+}} + X_{\mathrm{F^+}} = \eta \tag{25}$$

In the preceding equation, $\eta = M_I/M_A$ is the total propellant ionization fraction and W_s represents the molecular weight of each species. We further assume that the ion and neutral drift (mean) velocities at the thruster exit are uniform and steady, that is, $u_i(R, Z_E, t) = U_i$ and $u_n(R, Z_E, t) = U_n$. Therefore, the impulse bit is

$$I_{\mathrm{bit}} = \sum_i M_i u_i + \sum_n M_n u_n = M_I U_i + M_N U_n \tag{26}$$

Both I_{bit} and M_A are readily available from experiments. Therefore, specifying $\eta = M_I/M_A$ and $X_{\mathrm{C^+}}$, Eqs. (21–25) provide X_{C}, $X_{\mathrm{F^+}}$, and X_{F}. Given M_I and U_i, the impulse-bit equation (26) can be used to determine M_N and U_n.

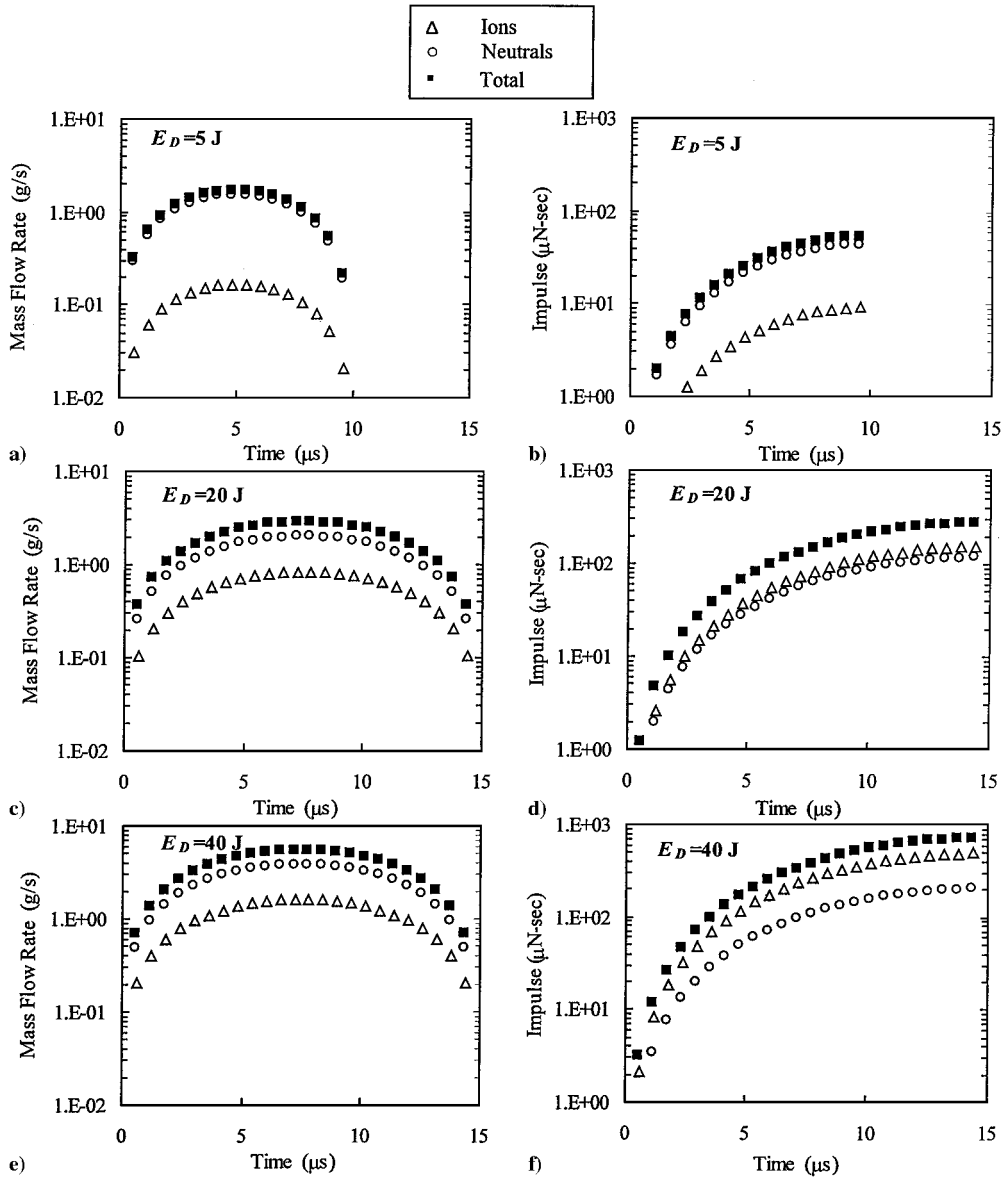

Fig. 3 Parameters derived from exit (injection) model used in simulations of GRC laboratory-model PPT plume.

To determine the number density we use the definition of the total ion mass injected during the pulse

$$M_I = \sum_i \int_P \dot{m}_i(t)\,\mathrm{d}t = \sum_i \int_P \int_A W_i \dot{N}_i(R, Z_\mathrm{E}, t)\,\mathrm{d}A\,\mathrm{d}t \quad (27)$$

A similar expression holds for the total neutral mass M_N. We further assume that the number density of species can be expressed as a product

$$n_s(R, Z_E, t) = n_s(t)Y(R, Z_E) \quad (28)$$

where $n_s(t)$ describes the time variation and $Y(R, Z_E)$ is a nondimensional function describing the radial variation of the density. The density used is a product of a sinusoidal and parabolic profile

$$n_s(R, Z_E, t) = n_{s,\max} \sin[(\pi/P)(t - t_1)]\left[1 - (1 - C_c)(R/R_T)^2\right]$$
$$t_1 \le t \le t_2 \quad (29)$$

where $P = t_2 - t_1$ is the duration of the pulse, R_T the equivalent radius of the thruster exit, and C_c the cutoff density ratio. The assumed sinusoidal time variation $n_s(t)$ follows the evolution of the PPT discharge current as well as the electron density variation at the near-exit region of the PPT. The radial variation is based on PPT channel simulations that indicate that density profiles are parabolic.[38] Substitution of Eq. (29) into Eq. (20) and use of Eq. (27) provides $n_{s,\max}$ as

$$n_{s,\max} = M_s \Big/ \Big(\tfrac{1}{4} W_s \bar{c}_s \Big\{\exp\big(-S_s^2\big) + \sqrt{\pi} S_s [1 + \mathrm{erf}(S_s)]\Big\} P(1 + C_c) R_T^2\Big) \quad (30)$$

Therefore, the number density $n_s(R, Z_E, t)$ and the number flux $\dot{N}_s(R, Z_E, t)$ can be completely determined. This thruster exit model accounts for the experimental impulse bit and total mass ablated during a pulse. Thrust and energy are also evaluated at the exit to compare with experimental data. This computation is performed at each time step to reproduce the unsteady injection process.

Results and Discussion

A series of simulations is performed using the GRC laboratory-model PPT shown schematically in Fig. 2. The objectives of these simulations are to explore the physical characteristics of the PPT plume, to validate the hybrid model by comparing simulation results with triple Langmuir probe data,[6,7] and to use the model to obtain

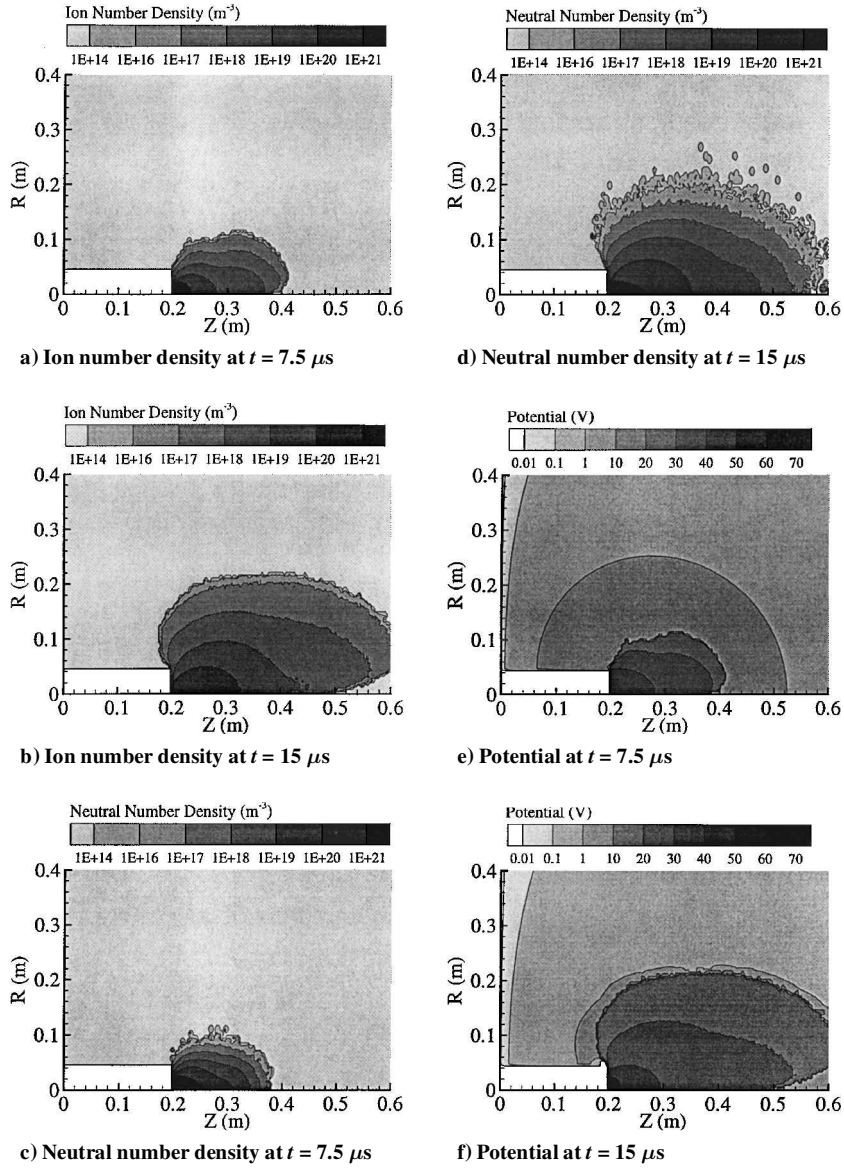

a) Ion number density at $t = 7.5\ \mu$s

d) Neutral number density at $t = 15\ \mu$s

b) Ion number density at $t = 15\ \mu$s

e) Potential at $t = 7.5\ \mu$s

c) Neutral number density at $t = 7.5\ \mu$s

f) Potential at $t = 15\ \mu$s

Fig. 4 Evolution of plasmoid during pulse from simulation of 20-J PPT plume.

backflow predictions for discharge energy of 5, 20, and 40 J. The laboratory-model PPT is a derivative of the LES-8/9, has parallel electrodes, and includes a housing. Figure 2 shows the triple-probe location during the experiments. Electron density was obtained in the plume on a plane parallel and perpendicular to the PPT electrodes for radial distances of 6–20 cm downstream with respect to the Teflon propellant and polar angles of 10, 20, 30, and 45 deg.

The axisymmetric simulation domain shown in Fig. 1 extends to $L_Z = 1$ m and $L_R = 1$ m in the axial and radial directions, respectively, and the surface has $Z_{S/C} = 0.2$ m and $R_{S/C} = 5 \times 10^{-2}$ m. The equivalent radius of the thruster is set to $R_T = 2.33 \times 10^{-2}$ m so that the simulation exit area equals that formed by the electrode distance (3.8×10^{-2} m) and the PPT housing width (4.5×10^{-2} m). The measured, assumed, and calculated parameters using the thruster exit (injection) model are shown in Table 2. The assumed parameters are chosen carefully and are consistent with current knowledge of PPT internal and plume flows. The plume composition is based on complete ablation of Teflon given in Eq. (21), but inclusion of additional species would not affect the overall evolution of the plume. The ionization fraction and ion speed are taken so that the derived exit-model ion number densities are close to the measured ones in the plume. The neutral temperature is based partially on the assumption that neutrals do not exceed their sonic speed at the PPT exit. Finally, the ion temperature is set to equal that of the neutrals,

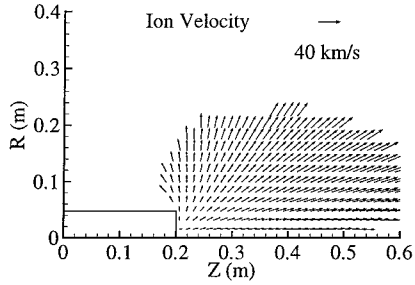

a) Ions

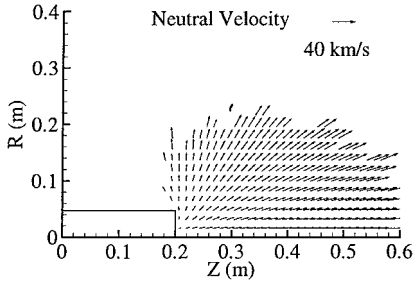

b) Neutrals

Fig. 5 Average (fluid) velocity field at end of pulse, t = 15 μs, from simulation of a 20-J PPT plume.

Table 2 Parameters used as inputs in the GRC PPT plume simulations

Parameter	Values		
	Known parameters		
E_D, J	5	20	40
A, m^2	17.1×10^{-4}	17.1×10^{-4}	17.1×10^{-4}
P, s	10×10^{-6}	15×10^{-6}	15×10^{-6}
I_{bit}, (μN · s)	36	256	684
M_A, kg	10.6×10^{-6}	26.6×10^{-6}	51.3×10^{-6}
	Assumed parameters		
s	C, F, C$^+$, F$^+$	C, F, C$^+$, F$^+$	C, F, C$^+$, F$^+$
M_I, kg	1.06×10^{-6}	7.98×10^{-6}	15.4×10^{-6}
U_i, m/s	8×10^3	20×10^3	34×10^3
$T_i(R, Z_E)$, eV	1	1	1
$T_n(R, Z_E)$, eV	1	1	1
	Derived parameters		
M_N, kg	9.54×10^{-6}	18.6×10^{-6}	35.9×10^{-6}
U_n, m/s	2.89×10^3	5.18×10^3	4.48×10^3
$n_{C^+,\max}$, m^{-3}	3.19×10^{20}	8.56×10^{20}	9.71×10^{20}
$n_{F^+,\max}$, m^{-3}	2.02×10^{20}	2.7×10^{20}	3.06×10^{20}
$n_{C,\max}$, m^{-3}	3.12×10^{21}	6.57×10^{20}	1.45×10^{21}
$n_{F,\max}$, m^{-3}	7.67×10^{21}	6.88×10^{21}	1.53×10^{22}

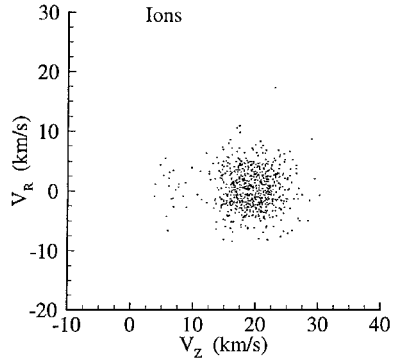

a) Ions at t = 1.5 μs

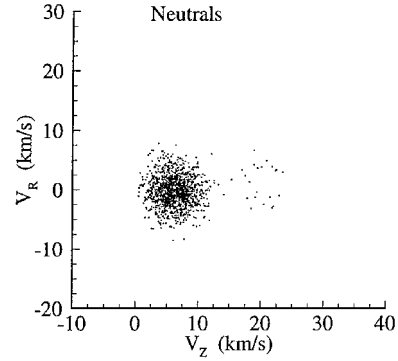

c) Neutrals at t = 1.5 μs

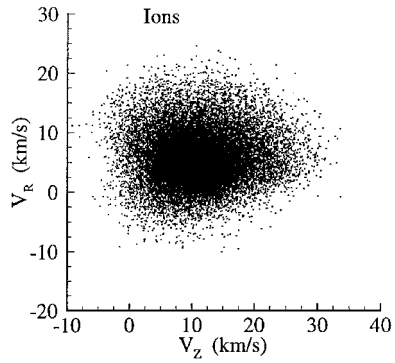

b) Ions at t = 15 μs

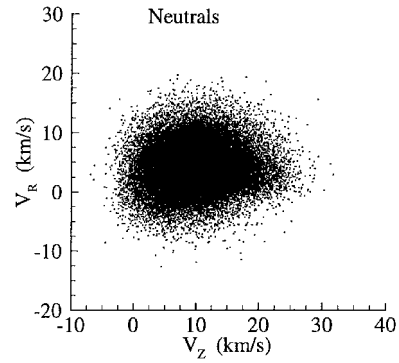

d) Neutrals at 15 ms

Fig. 6 Particle velocity phase space ($V_Z - V_R$) from simulation of 20-J PPT plume.

although as a parameter it plays a secondary role due to the supersonic speed of the ions. The background densities in the tank could reach 5×10^{17} m^{-3}, resulting in $\lambda_{nn} > 3$ m and $\tau_{nn} > 2 \times 10^{-3}$ s for neutral–neutral collisions and $\lambda_{\text{in}} > 25$ m and $\tau_{\text{in}} > 20 \times 10^{-3}$ s for plume ion/background neutral collisions. This implies that background neutrals do not affect the plume expansion for the timescales of less than 20 μs and length scales of smaller than 1 m considered in our simulations. As such, the background neutral density was set to $n_{n0} = 10^{15}$ m^{-3} and $n_{e0} = n_{i0} = 10^{12}$, simulating the largest background density that could be encountered in LEO.

The axisymmetric nonuniform grid used in the simulations has $N_Z + 1$ and $N_R + 1$ grid points in the axial and radial directions, respectively. The axial and radial widths of the (i, j)th cell are based on a geometric series given by

$$\Delta Z_i = L_Z \frac{1 - A_Z^{1/(N_Z-1)}}{1 - A_Z^{N_Z/(N_Z-1)}} A_Z^{(i-1)/(N_Z-1)} \qquad \text{for} \qquad i = 1, N_Z \tag{31}$$

$$\Delta R_j = L_R \frac{1 - A_R^{1/N_R - 1}}{1 - A_R^{N_R/(N_R-1)}} A_R^{(j-1)/(N_R-1)} \qquad \text{for} \qquad j = 1, N_R \tag{32}$$

where $A_Z = \Delta Z_{N_Z}/\Delta Z_1$ and $A_R = \Delta R_{N_R}/\Delta R_1$. The last-to-first cell ratios A_Z and A_R are set to values so that widths of the cells in the downstream region of the PPT exit scale with the smallest mean-free paths expected during the plasmoid propagation. To account for the downstream propagation of the dense plasmoid, the cell width is kept nearly uniform in the axial direction and is stretched in the radial direction. In the simulations $L_Z = L_R = 1$ m, $N_Z = 320$, $N_R = 150$, $A_Z = 1.0795$, and $A_R = 2.7859$. With these values, $\Delta Z_{\min} = 3.007 \times 10^{-3}$ m, $\Delta R_{\min} = 3.822 \times 10^{-3}$ m, $\Delta Z_{\max} = 3.246 \times 10^{-3}$ m, and $\Delta R_{\max} = 10.648$ mm. The cells are also divided into four subcells in both directions and used for sampling of collision partners. The most restrictive densities in terms of required grid resolution occur next to the PPT exit at the peak of the pulse. For the conditions listed in Table 2, $n_{\text{C,max}} = 3.12 \times 10^{21}$ m^{-3}, $n_{\text{F,max}} = 1.53 \times 10^{22}$ m^{-3}, and the smallest mean-free paths are $\lambda_{\text{C}^+,\text{C}}^{\text{CEX}} \approx 3 \times 10^{-4}$ m, $\lambda_{\text{C,C}} \approx 9 \times 10^{-4}$ m, $\lambda_{\text{F}^+,\text{F}}^{\text{CEX}} \approx 1.5 \times 10^{-4}$ m, and $\lambda_{\text{F,F}} \approx 2 \times 10^{-4}$ m. The dimensions of the subcells next to the PPT exit are 7.5×10^{-4} m in the Z direction and 9.59×10^{-4} in the R direction. Therefore, the subcells at the exit region are of the order of the most restrictive mean-free paths that occur at the density peak. For the rest of the pulse, the maximum neutral densities next to the PPT exit, as well as downstream, are always smaller than their peak values, and, therefore, the cell and subcell dimensions used in the

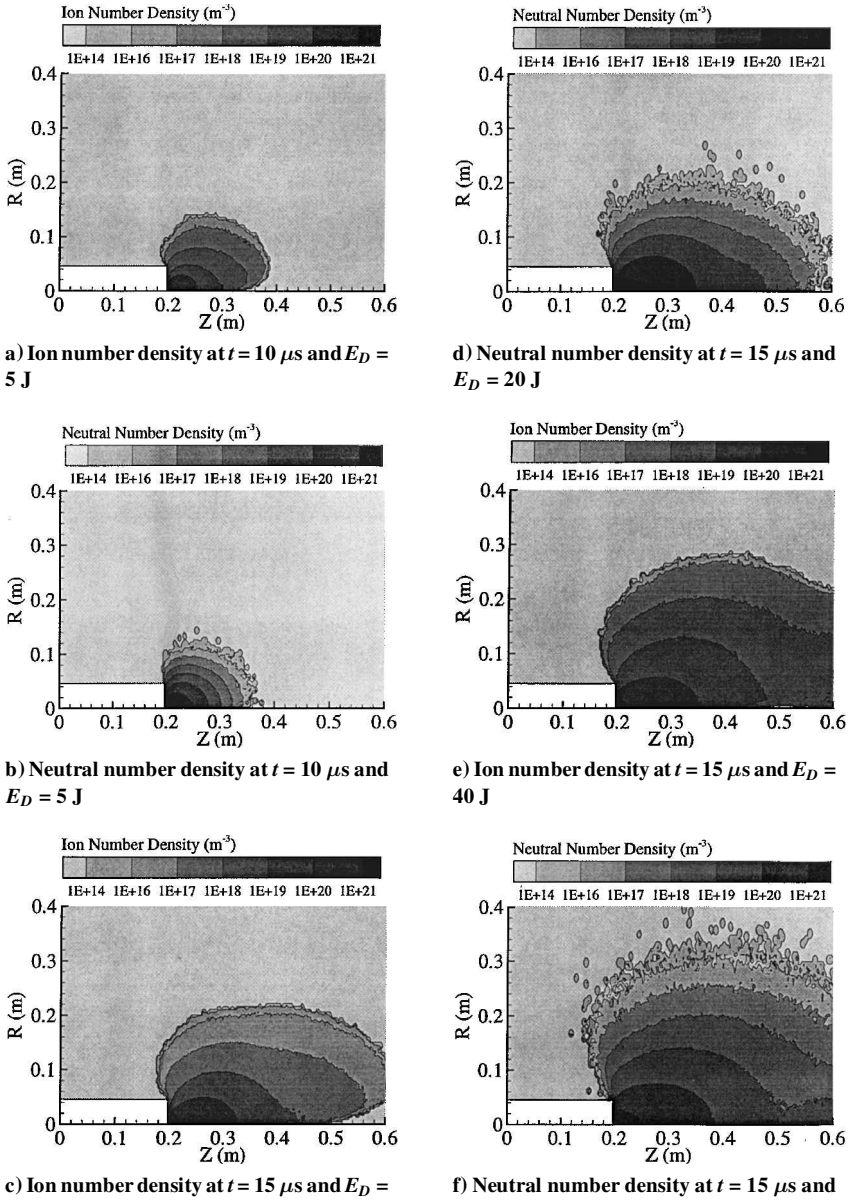

a) Ion number density at $t = 10$ μs and $E_D = 5$ J

b) Neutral number density at $t = 10$ μs and $E_D = 5$ J

c) Ion number density at $t = 15$ μs and $E_D = 20$ J

d) Neutral number density at $t = 15$ μs and $E_D = 20$ J

e) Ion number density at $t = 15$ μs and $E_D = 40$ J

f) Neutral number density at $t = 15$ μs and $E_D = 40$ J

Fig. 7 Simulation results of PPT plume showing plasmoid at the end of a pulse for various discharge energy levels.

simulations are smaller than the mean-free paths. The total number of computational particles at the end of the pulse is 480,590 ions and 3,920,001 neutrals for the 5-J case; 1,271,338 ions and 2,525,192 neutrals for the 20-J case; and 1,258,637 ions and 1,339,862 neutrals for the 40-J case. The number of real to computational particles is 8.3×10^{10} for the 5-J, 2.5×10^{11} for the 20-J, and 5×10^{11} for the 40-J cases. Time steps are $\Delta t_i = 0.05\ \mu$s and $\Delta t_n = 0.1\ \mu$s for all cases considered.

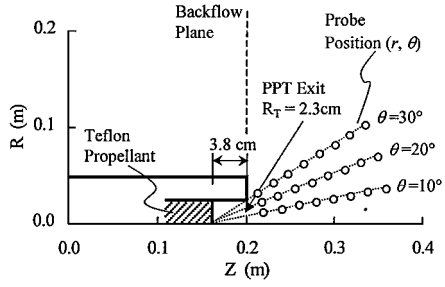

Fig. 8 Probe locations used in simulation; distance r and angle θ are referred to with respect to the center of the Teflon propellant for direct comparison with experiment.

The ion and neutral mass flow rates are shown in Fig. 3a for capacitor discharge energies of 5, 20, and 40 J. Clearly, neutrals are the dominant species for all three cases considered. The impulse obtained at the thruster exit during particle injection is shown in Fig. 3b. Figures 3a and 3b ensure that the injection model reproduces the measured total impulse bit. The contribution to the impulse bit from neutrals and ions is still an open issue and can only be addressed from experimental data at the thruster exit or detailed internal modeling.[38] These issues are outside of the scope of this paper.

Physical Characteristics of Plume

We investigate next the physical characteristics of the PPT plume using results from a simulation of the GRC PPT operating at 20 J. Figures 4a and 4b show the evolution of the ion component of the plasmoid, referred to as the ion cloud. At $t = 7.5\ \mu$s the ion cloud has reached 0.2 cm from the exit, but does not exhibit any backflow. At $t = 15\ \mu$s a backflow component appears, as well as significant expansion in the radial direction. The maximum ion density reaches 1×10^{21} m^{-3}. Figures 4c and 4d show the evolution of the neutral component of the plasmoid, referred to as the neutral cloud. A comparison between Figs. 4a and 4c shows the initially slower

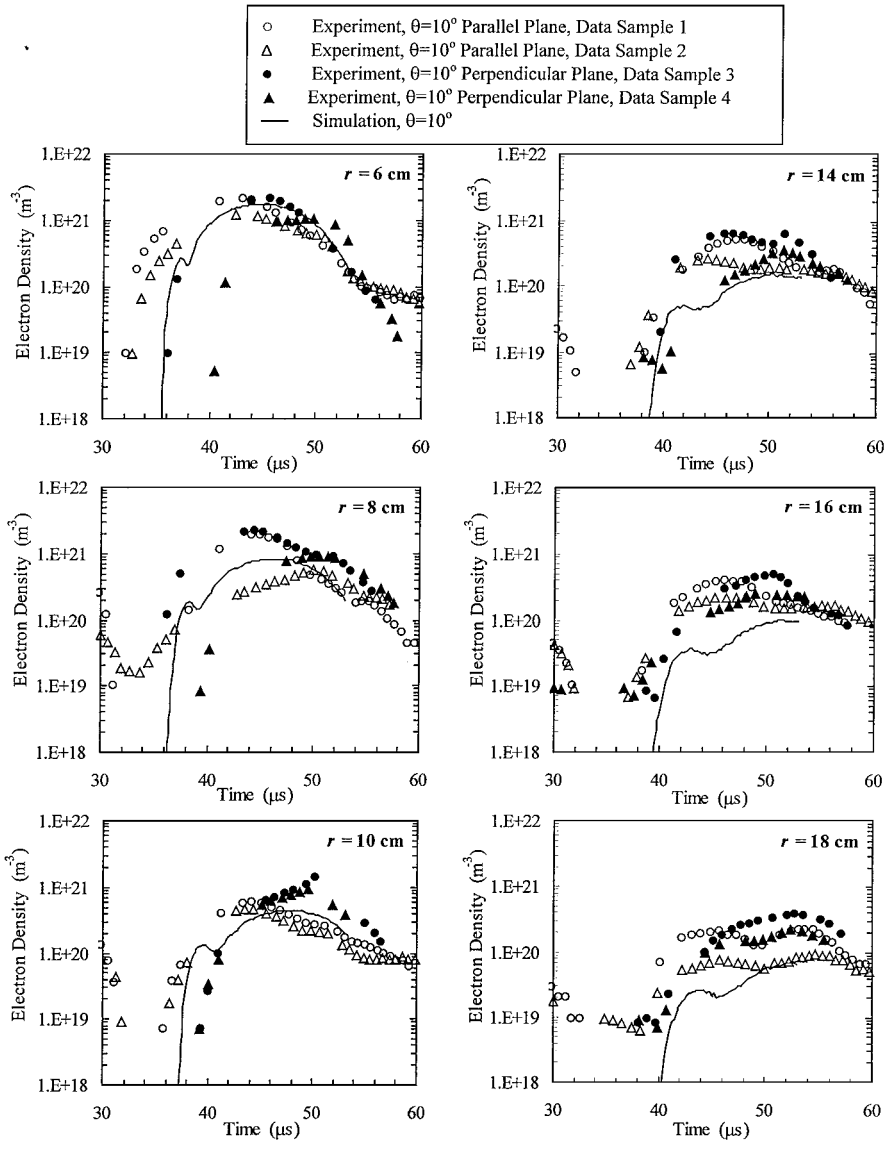

Fig. 9 Comparison between electron number density (per cubic meter) predictions and experimental data in the plume of 20-J GRC laboratory-model PPT; data are depicted along θ = 10 deg angle and for distances between 6 and 18 cm with respect to center of Teflon propellant, time is that of experiment.

evolution of the neutral cloud. However, at the end of the pulse the neutral and ion clouds almost reach the same axial downstream distance that Figs. 4b and 4d show. This faster expansion can be attributed to the presence of fast CEX neutrals. Figure 4d shows that at $t = 15$ μs the neutral cloud expands in both the radial and backflow region. Figures 4e and 4f show the evolution of the potential field. The structure follows the morphology of the ion cloud as a comparison between Figs. 4a and 4b or Figs. 4e and 4f shows. The maximum values of the potential scale with $\varphi \approx T_e \ln(n_{e,\max}/n_{e0})$ and are collocated with the density maxima.

Figures 5a and 5b display the ion and neutral (fluid or mass average) velocity vectors at $t = 15$ μs. Only a percentage of the total number of vectors is depicted for clarity. The plot shows that ions exhibit larger backflow velocities as compared to neutrals. This can be attributed to the presence of electric fields that turn the slow energy plume ions toward the backflow region.

Figure 6 displays the phase plots ($v_Z - v_R$) of the ion and neutral distribution functions. At $t = 1.5$ μs the ion (Fig. 6a) and neutral phase space (Fig. 6c) display the flow parameters of the injection according to Table 2. At the end of the pulse the appearance of a low-energy ion population is depicted in Fig. 6b. This population is the result of the CEX reactions between $C–C^+$ and $F–F^+$. As a result of the radial electric fields, the ionic population with large radial velocities increases. In addition, Fig. 6b shows backstreaming ions with negative axial velocities that belong to the low-energy CEX population exclusively. Figures 6c and 6d show similar phase plots for the neutrals. The neutrals injected with 5.18-kms^{-1} drift develop a population with high axial velocities due to CEX. In addition, neutrals expand in the radial direction as Fig. 6d depicts, and neutral backflow is predicted due to the population with negative axial velocities. A comparison between Figs. 6b and 6d shows that ions develop larger radial speeds than the neutrals due to the radial electric fields in the plasmoid.

Similar simulations were performed for the 5 and 40-J PPT to examine the evolution of the plasmoid and the effects of discharge energy. Figure 7 shows the ion and neutral number density at the end of the PPT pulse for the three energy levels considered. The 5-J plume in Figs. 7a and 7b shows the least spatial extension due to the lowest ablated mass and pulse duration. A comparison between Figs. 7c and 7d shows that the spatial expansion of the ion and neutral components of the plasmoid increases with increasing discharge energy. This is a direct result of the increase in the ablated mass. In addition, all cases show the development of ion and neutral backflow.

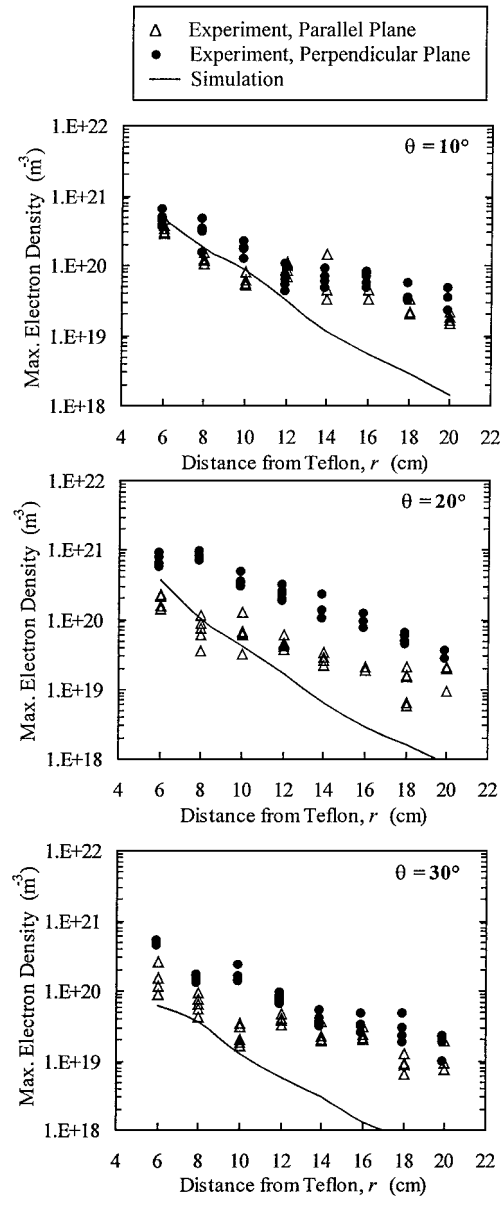

Fig. 10 Comparison between predicted and measured maximum electron number density (per cubic meter) in the plume of GRC laboratory-model PPT with $E_D = 5$ J; distances are measured with respect to Teflon propellant.

Comparisons with Experiments

A series of comparisons is performed next, between electron density predictions and our triple Langmuir probe plume data.[6,7] Figure 8 shows the location of the simulation probes. To compare with the experiment shown in Fig. 2, a polar coordinate system (r, θ) is used where distances and polar angles are referred to with respect to the center of the Teflon propellant, which is located 3.8 cm behind the PPT exit.

Figure 9 shows the time evolution of the electron number density along the $\theta = 10$ deg line and distances from the Teflon propellant between 6 and 18 cm for the $E_D = 20$ J case. In Fig. 9, two data sets are plotted for each plane to indicate the pulse-to-pulse variation of density during the experiments, as well as the density differences between the planes parallel and perpendicular to the PPT electrodes. The time depicted in Fig. 9 is that of the experiment and was measured relative to the triggering of each triple-probe data set collection. Therefore, the experiment time does not coincide with the initiation of the discharge and is important only in terms of the relative time difference because triggering was varied from one PPT discharge to the other. To facilitate the comparisons, the simulation $t = 0$ μs corresponds to approximately $t_{\exp} = 35$ μs. Figure 9 shows clearly that the simulation results follow the data closely for all radial distances considered. The maximum of the density decreases with radial distance due the expansion and the plasmoid spreads due to diffusion. Note that due to the unsteady exit conditions of the PPT, such density comparisons are not trivial as would be the case of a thruster operating in steady mode. Figure 9 shows that for $r = 6$ cm at about 37 μs (or 2 μs in simulation time) the electron (and ion) density decrease from about 2.6×10^{20} to 2.2×10^{20} m^{-3} despite the expected monotonic increase due to sinusoidal injection profile. This density perturbation is generated with the onset of CEX collisions in the near exit region as a result of the increased radial removal rate of the slow CEX ions. This density perturbation is then convected downstream and is shown at distances of 8, 10, and 12 cm to reduce in magnitude and spread wider due to diffusion. The very small magnitude of this density perturbation does not affect the evolution of the plasmoid or the results of these computations.

To summarize model/experiment comparisons, we plot in Figs. 10–12 the maximum electron density during the pulse for radial distances between 6 and 20 cm and angles $\theta = 10$, 20, and 30 deg. The measured density maxima are shown for the parallel and perpendicular planes to show the variability in the data.

Figure 10 shows that, for the 5-J case, numerical predictions are of the same order as measurements for distances of up to $r = 12$ cm.

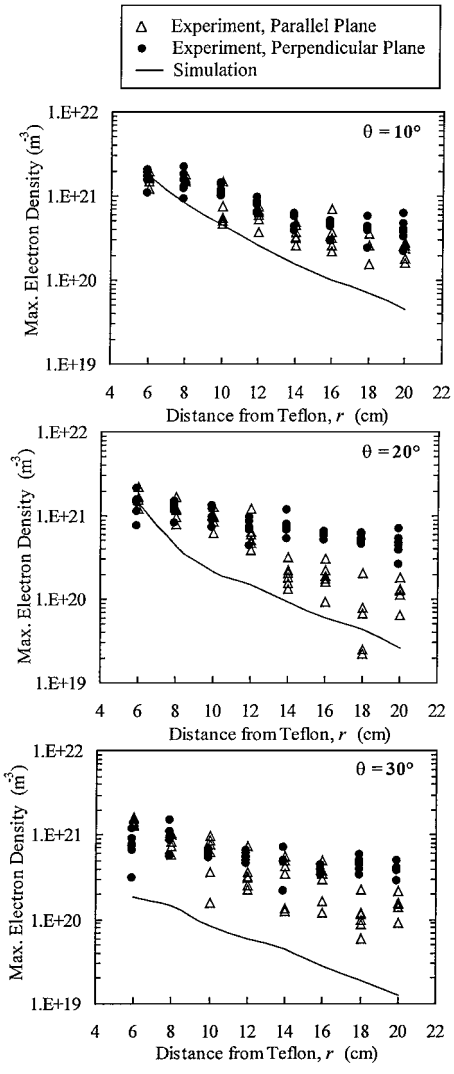

Fig. 11 Comparison between predicted and measured maximum electron number density (per cubic meter) in the plume of GRC laboratory-model PPT with $E_D = 20$ J; distances are measured with respect to center of Teflon propellant.

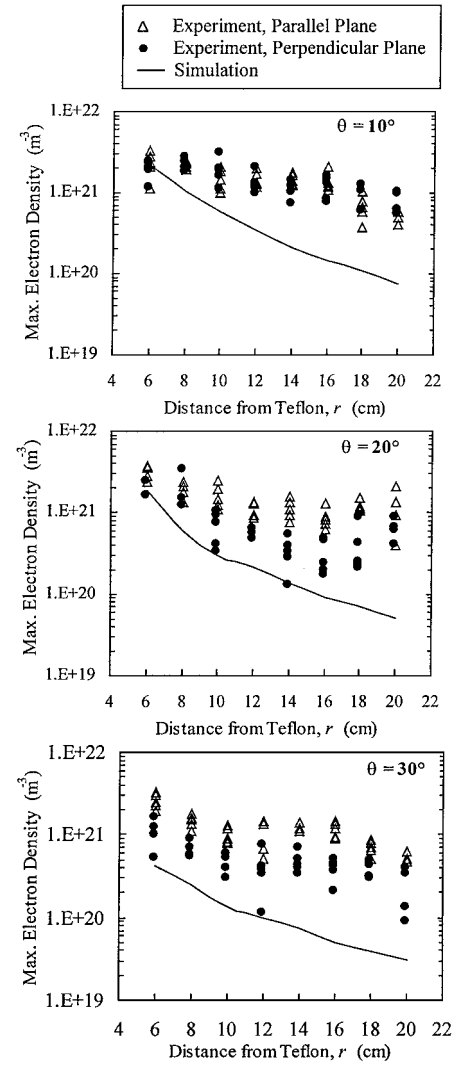

Fig. 12 Comparison between predicted and measured maximum electron number density (per cubic meter) in the plume of GRC laboratory-model PPT with $E_D = 40$ J; distances are measured with respect to center of Teflon propellant.

The underprediction increases with distance from the Teflon, and for $r = 20$ cm the numerical value is an order of magnitude smaller than the measurements. Figure 11 shows that the 20-J case numerical predictions are smaller by less than an order of magnitude for distances of up to $r = 20$ cm and for $\theta = 10$ and 20 deg. For $\theta = 30$ deg, the density maxima are underpredicted for all distances and become smaller than measurements by an order of magnitude at distances beyond 14 cm. The 40-J case numerical predictions shown in Fig. 12 are smaller than measurements by less than an order of magnitude for all distances and angles.

There are several possible explanations for these differences between numerical predictions and the experiment. Facility effects, especially electrical coupling of the plasma with the walls of the small, 0.5×1 m cylindrical chamber used in our experiments may have inhibited the expansion of the plasmoid. Triple langmuir probe misalignment with the flow vector may also have resulted in an overestimation of the electron density, especially at large angles. Note that experimental number densities have an uncertainty of 60%, assuming perfectly aligned probes.[6] In addition, inaccuracies in model assumptions, as well as input conditions, may have attributed to these underpredictions. The comparisons also show that the axisymmetric simulations fail to capture the three dimensionality of the plume exhibited by the density differences between the parallel and perpendicular planes shown in Figs. 9–12.

Backflow Estimates

To quantify the effects of PPT energy level on backflow, the mass of ion and neutral propellant through the backflow plane shown in Fig. 2 is evaluated. The backflow mass of a species s and time t is defined as

$$M_s^B(t) = \int_0^t \int_{A_B} \dot{N}_s(R_B, Z_B, t)\, \mathrm{d}A\, \mathrm{d}t \tag{33}$$

and the injected mass is defined as

$$M_s(t) = \int_0^t \dot{m}_s(t)\, \mathrm{d}t \tag{34}$$

Figure 13 shows the evolution of $M_I^B(t)$, $M_N^B(t)$, $M_I(t)$, and $M_N(t)$ for the 5-, 20-, and 40-J cases, respectively. Backflow begins at about midpulse for all three cases considered. Note that this picture is associated with a single PPT pulse. A PPT firing includes many pulses, and in that case the picture of the backflow would be substantially different. The comparison between backflow and injected mass during a single PPT pulse is presented in Fig. 14. The total backflow mass is a fraction of the ablated and is $5.45 \times 10^{-3}\,\mu$g, $1.4 \times 10^{-2}\,\mu$g, and $0.1\,\mu$g for the 5-, 20-, and 40-J cases, respectively.

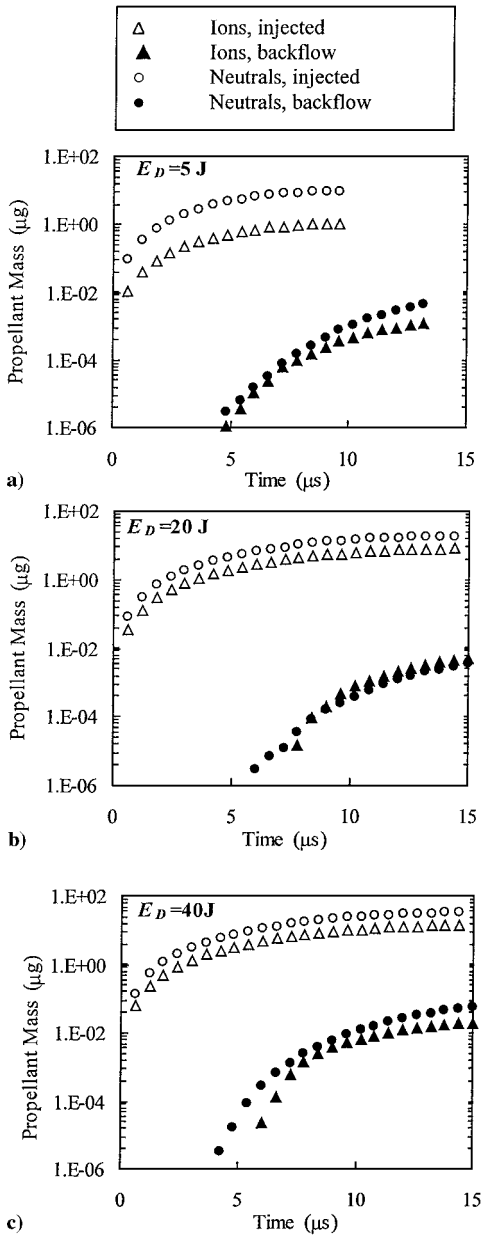

Fig. 13 a) Evolution of injected and backflow propellant mass from simulation of 5-J PPT plume, b) evolution of injected and backflow propellant mass from simulation of 20-J PPT plume, c) evolution of injected and backflow propellant mass from simulation of 40-J PPT plume.

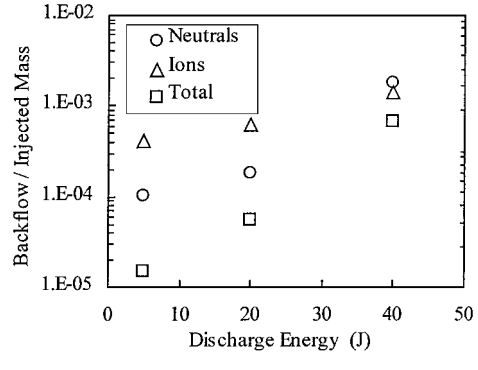

Fig. 14 Comparison of backflow and injected propellant mass from PPT simulations.

Summary

In this study we presented a hybrid physical and computational model for the partially ionized PPT plume. This modeling effort, along with plume characterization efforts, enhances our understanding of the physical processes occurring in PPT plumes and provides a prediction ability that will address PPT/spacecraft integration issues.

The hybrid computational methodology is based on a combination of the DSMC, hybrid-PIC, and fluid approaches. Simulations using operating conditions of the GRC laboratory-model PPT with discharge energy of 5, 20, and 40 J revealed important characteristics of the plume. Simulations show the expansion of the neutral and ion components of the plasmoid and the generation of backflow. The model predicts the generation of low-energy ions and high-energy neutrals due to CEX reaction. The presence of these components needs to be verified with experiments. Estimates of backflow show the effects of discharge energy (and ablated mass). Comparisons of the electron density evolution predicted by the model for the 20-J PPT show good agreement with triple langmuir probe data. Model predictions of the maximum electron density during the pulse are within the same order of magnitude, with measurements for radial distances of up to 12 cm from the Teflon and angles of $\theta = 10$ and 20 deg from the centerline for the three discharge energy levels considered. In general, the under-prediction of the density maxima increase with increasing distance from the Teflon and increasing angle off the centerline. Differences between numerical and experimental densities can be attributed to uncertainties in the triple langmuir probe data, flow-triple probe misalignment at off-axis locations that may have resulted in an overestimation of the electron density, small-chamber effects that may have inhibited the rapid expansion of the plasmoid, and model inaccuracies.

Current work is devoted to expanding the methodology into three dimensions to capture the asymmetry of the PPT plume and to adding an energy equation to account for the temperature evolution due to the plasmoid expansion.

Acknowledgments

This work was performed under Grant NAG3-1873 sponsored by NASA John H. Glenn Research Center at Lewis Field.

References

[1]Gatsonis, N. A., and Yin, X., "Axisymmetric DSMC/PIC Simulation of Quasineutral Partially Ionized Jets," AIAA Paper 97-2535, June 1997.

[2]Gatsonis, N. A., and Yin, X., "Theoretical and Computational Analysis of Pulsed Plasma Thruster Plumes," IEPC Paper 97-041, Aug. 1997.

[3]Gatsonis, N. A., and Yin, X., "Hybrid (Fluid/PIC/DSMC) Simulation of Partially Ionized Jets," *Rarefied Gas Dynamics*, edited by R. Brun, R. Campargue, R. Catignol, and J. C. Lengrand, Vol. II, Cepadues-Editions, Toulouse, France, 1999, pp. 393–400.

[4]Myers, R. M., Arrington, L. A., Pencil, E. J., Carter, J., Heminger, J., and Gatsonis, N. A., "Pulsed Plasma Thruster Contamination," AIAA Paper 96-2729, July 1996.

[5]Eckman, R., Gatsonis, N., Myers, R., and Pencil, E., "Experimental Investigation of the LES 8/9 Pulsed Plasma Thruster Plume," IEPC Paper 97-126, International Electric Propulsion Conf., Aug. 1997.

[6]Eckman, R., Byrne, L., Gatsonis, N. A., and Pencil, E. J., "Triple Langmuir Probe Measurements in the Plume of a Pulsed Plasma Thruster," *Journal of Propulsion and Power*, Vol. 17, No. 4, 2001, pp. 762–771.

[7]Eckman, R., "Langmuir Probe Measurements in the Plume of a Pulsed Plasma Thruster," M.S. Thesis, Mechanical Engineering Dept., Worcester Polytechnic Inst., Worcester, MA, Feb. 1999.

[8]Vondra, R. J., Thomassen, K. I., and Solbes, A., "Analysis of Solid Teflon Pulsed Plasma Thruster," *Journal of Spacecraft and Rockets*, Vol. 7, No. 12, 1970, pp. 1402–1406.

[9]Vondra, R. J., Thomassen, K. I., and Solbes, A., "A Pulsed Electric Thruster for Satellite Control," *Proceedings of the IEEE*, Vol. 59, No. 2, 1971, pp. 271–277.

[10]Thomassen, K. I., and Vondra, R. J., "Exhaust Velocity Studies of a Solid Teflon Pulsed Plasma Thruster," AIAA Paper 71-94, Jan. 1971.

[11]Thomassen, K. I., and Tong, D., "Interferometric Density Measurements in the Arc of a Pulsed Plasma Thruster," *Journal of Spacecraft and Rockets*, Vol. 10, No. 3, 1973, pp. 163, 164.

[12]Guman, W. J., and Begun, M., "Exhaust Plume Studies of a Pulsed Plasma Thruster," AIAA Paper 97-704, April 1978.

[13]Rudolph, L. K., Harstad, K. G., Pless, L. C., and Jones, R. M., "Plume Characterization of a One-Millipound Solid Teflon Pulsed Plasma Thruster," U.S. Air Force Rocket Propulsion Lab. TR-79-60, Sept. 1979; also NASA CR-162786, Sept. 1979.

[14]Dawbarn, R., McGuire, R. L., Steely, S. L., and Pipes, J. G., "Operating Characteristics of an Ablative Pulsed Plasma Engine," Arnold Engineering Development Center TR-82-9, 1982.

[15]Hirata, M., and Murakami, H., "Exhaust Gas Analysis of a Pulsed Plasma Engine," IEPC Paper 84-52, 1984.

[16]Burton, R. L., and Turchi, P. J., "Pulsed Plasma Thruster," *Journal of Propulsion and Power*, Vol. 14, No. 5, 1998, p. 716.

[17]Spanjers, G. G., Malak, J. B., Leiweke, R. J., and Spores, R. A., "Effect of Propellant Temperature in the Pulsed Plasma Thruster," *Journal of Propulsion and Power*, Vol. 14, No. 4, 1998, pp. 545–553.

[18]Spanjers, G. G., Lotspeich, J. S., McFall, K. A., and Spores, R. A., "Propellant Losses Because of Particulate Emission in a Pulsed Plasma Thruster," *Journal of Propulsion and Power*, Vol. 14, No. 4, 1998, pp. 554–559.

[19]Ebert, W. L., Kowal, S. J., and Sloan, R. F., "Operational NOVA Spacecraft Teflon PPT System," AIAA Paper 89-2497, July 1989.

[20]Bird, G. A., *Molecular Gas Dynamics and the Direct Simulation of Gas Flows*, Clarendon, Oxford, England, U.K., 1994.

[21]Elgin, J. B., Cooke, D. C., Tautz, M. F., and Murad, E., "Modeling of Atmospherically Induced Gas Phase Optical Contamination for Orbiting Spacecraft," *Journal of Geophysical Research*, Vol. 95, No. A8, 1990, pp. 12197–12208.

[22]Boyd, I. D., Penko, P. F., and Meissner, D. L., "Experimental and Numerical Investigations of Low-Density Nozzle and Plume Flows of Nitrogen," *AIAA Journal*, Vol. 30, No. 10, 1992, pp. 2453–2461.

[23]Rault, D. F. G., and Woronowicz, M. S., "Application of Direct Simulation Monte Carlo to Satellite Contamination Studies," *Journal of Spacecraft and Rockets*, Vol. 32, No. 3, 1995, p. 392.

[24]Ivanov, M. S., Markelov, G. N., Gerasimov, Y. I., Krylov, A. N., Mishina, L. V., Sokolov, E. I., "Free-Flight Experiment and Numerical Simulation for Cold Thruster Plume," *Journal of Propulsion and Power*, Vol. 15, No. 3, 1999, pp. 417–423.

[25]Gatsonis, N. A., Nanson, R., and LeBeau, J., "Simulations of Cold-Gas Nozzle and Plume Flows and Flight Data Comparisons," *Journal of Spacecraft and Rockets*, Vol. 37, No. 1, 2000, pp. 39–48.

[26]Birdsall, C. K., and Langdon, A. B., *Plasma Physics Via Computer Simulation*, McGraw–Hill, New York, 1992.

[27]Hockney, R. W., and Eastwood, J. W., *Computer Simulation Using Particles*, Adam Hilger, New York, 1988.

[28]Samanta Roy, R. I., Hastings, D. E., and Gatsonis, G. A., "Ion-Thruster Plume Modeling for Backflow Contamination," *Journal of Spacecraft and Rockets*, Vol. 33, No. 4, 1996, pp. 525–534.

[29]Samanta Roy, R. I., Hastings, D. E., and Gatsonis, G. A., "Numerical Simulation of Spacecraft Contamination and Interactions by Ion-Thruster Effluents," *Journal of Spacecraft and Rockets*, Vol. 33, No. 4, 1996, pp. 535–542.

[30]Gatsonis, N. A., Yin, X., and Buzby, J., "Particle Simulation of Partially Ionized Hydrogen Plumes," *Rarefied Gas Dynamics*, edited by Ching Shen, Peking Univ. Press, Beijing, China, 1997, pp. 561–566.

[31]Oh, D., "Modeling of Stationary Plasma Thruster-100 Thruster Plumes and Implications for Satellite Design," *Journal of Propulsion and Power*, Vol. 15, No. 2, 1999, pp. 345–357.

[32]VanGilder, D. B., Boyd, I. D., and Keidar, M., "Particle Simulations of a Hall Thruster Plume," *Journal of Spacecraft and Rockets*, Vol. 37, No. 1, 2000, pp. 129–136.

[33]Gatsonis, N. A., and Hastings, D. E., "Evolution of the Plasma Environment Induced Around Spacecraft by Gas Releases: Three-dimensional Modeling," *Journal of Geophysical Research*, Vol. 97, No. A10, 1992, pp. 14989–15005.

[34]Jones, M. E., Lemons, D. S., Mason, R. J., Thomas, V. A., and Winske, D., "A Grid-Based Coulomb Method for PIC Codes," *Journal of Computational Physics*, Vol. 123, No. 1, 1996, pp. 169–181.

[35]Banks, P., "Collision Frequencies and Energy Transfer: Ions," *Planetary and Space Science*, Vol. 14, No. 1104, 1968, pp. 1085–1103.

[36]Lieberman, M. A., and Lichtenberg, A. J., *Principles of Plasma Discharges and Materials Processing*, Wiley, New York, 1994.

[37]Sakabe, S., and Izawa, Y., "Cross Sections for Resonant Charge Transfer Between Atoms and Their Positive Ions: Collision Velocity $\leq$1 a.u.," *Atomic and Nuclear Data Table*, Vol. 49, Academic, New York, 1991, pp. 257–314.

[38]Turchi, P. J., and Mikellides, P. G., "Modeling of Ablation-Fed Pulsed Plasma Thrusters," AIAA Paper 95-2915, July 1995.

[39]Ruyten, W. M., "Density-Conserving Shape Factors for Particle Simulations in Cylindrical and Spherical Coordinates," *Journal of Computational Physics*, Vol. 105, No. 2, 1993, pp. 224–232.

[40]Mitchner, M., and Kruger, C.H., Jr., *Partially Ionized Gases*, Wiley, New York, 1992.